




3D-Printed porous MnO₂/Carbon composites synthesized via fast joule heating for energy storage electrodes

Jun Cao^a, Chunjie Yan^a, Qi Sun^b, Xiaoyan Zhu^a, Sen Zhou^a, Ziming Song^a, Zhigang Wang^a, Heng Deng^{a,c,*} 

^a Faculty of Materials Science and Chemistry, China University of Geosciences, Wuhan 430074, People's Republic of China

^b College of Materials and Metallurgy, Guizhou University, Guiyang 550025, People's Republic of China

^c Shenzhen Research Institute, China University of Geosciences, Shenzhen 518000, People's Republic of China

ARTICLE INFO

Keywords:

3D printing
Fast Joule Heating
MnO₂
Supercapacitor
Lithium-ion batteries

ABSTRACT

Advanced energy storage technologies require electrodes with optimized structures to enhance performance. 3D printing has emerged as an innovative technique for combining conductive scaffolds and electroactive nanomaterials, offering precise control over electrode architecture and performance. To achieve optimal 3D printing results, ensuring strong and stable integration between the conductive scaffold and electroactive nanomaterials is essential. In this study, we present a novel approach for fabricating porous MnO₂/carbon composite electrodes using the fast joule heating (FJH), which transforms natural rhodochrosite and polyimide precursors into hierarchical MnO₂ nanoparticles anchored on carbon fibers under extreme conditions ($\approx 1800^\circ\text{C}$ in 1 s). This composite material exhibits robust interfacial bonding and high porosity, critical for superior electrochemical performance. The MnO₂/carbon composite is processed into a conductive ink for direct ink writing, enabling the fabrication of 3D-printed electrodes with tailored structures. The resulting electrodes demonstrate remarkable electrochemical performance, with a high specific capacitance of 411.3 mF cm^{-2} at 1.0 A g^{-1} for supercapacitors and a stable capacity of 570.9 mAh g^{-1} after 400 cycles for lithium-ion batteries, with 97.8 % coulombic efficiency. This work highlights the potential of combining FJH method and 3D printing for high-performance energy storage applications.

1. Introduction

In recent years, energy storage technologies, including supercapacitors (SCs) [1,2], lithium-ion batteries (LIBs) [3,4], sodium-ion batteries [5,6], and zinc-ion batteries (ZIBs) [7,8], have garnered significant attention for their critical role in the transition to a sustainable energy future. Central to the performance of these devices is the design and architecture of their electrodes, which directly influence energy density, power density, and cycling stability [9,10]. Among the various fabrication techniques, 3D printing has emerged as a groundbreaking method for fabricating electrodes with enhanced structural control and performance capabilities [11,12]. The precision of 3D printing allows for the creation of intricate, tailored architectures that maximize surface area, facilitate ion diffusion [13,14], and optimize mechanical robustness [15], all while minimizing material waste. As a result, 3D-printed electrodes offer significant advantages over conventional bulk electrodes, especially in terms of scalability, cost-effectiveness, and design

versatility [16,17].

3D-printed electrodes typically consist of two critical components: a conductive scaffold and electroactive nanomaterials. The conductive scaffold, often made from materials such as graphene [18], carbon nanotube [19] and MXenes [20], serves dual purposes—it provides the necessary electrical pathways for efficient electron transport and acts as a mechanical backbone to support the overall 3D structure. Meanwhile, the electroactive nanomaterials, which include transition metal oxides like MnO₂ [21], Co₃O₄ [22], and layered double hydroxides (LDHs) [23], enhance the electrode's electrochemical properties by contributing pseudocapacitance or faradaic activity. By combining these components, 3D-printed electrodes can achieve high electrochemical performance, with improved charge storage capacity, rate capability, and cycling stability. The fabrication of 3D-printed electrodes can generally be categorized into two approaches. The first approach involves printing the conductive scaffold first, followed by the deposition of electroactive nanomaterials onto the scaffold using methods such as

* Corresponding author at: Faculty of Materials Science and Chemistry, China University of Geosciences, Wuhan 430074, People's Republic of China.

E-mail address: dengheng@cug.edu.cn (H. Deng).

<https://doi.org/10.1016/j.cej.2025.159723>

Received 27 November 2024; Received in revised form 3 January 2025; Accepted 17 January 2025

Available online 18 January 2025

1385-8947/© 2025 Published by Elsevier B.V.

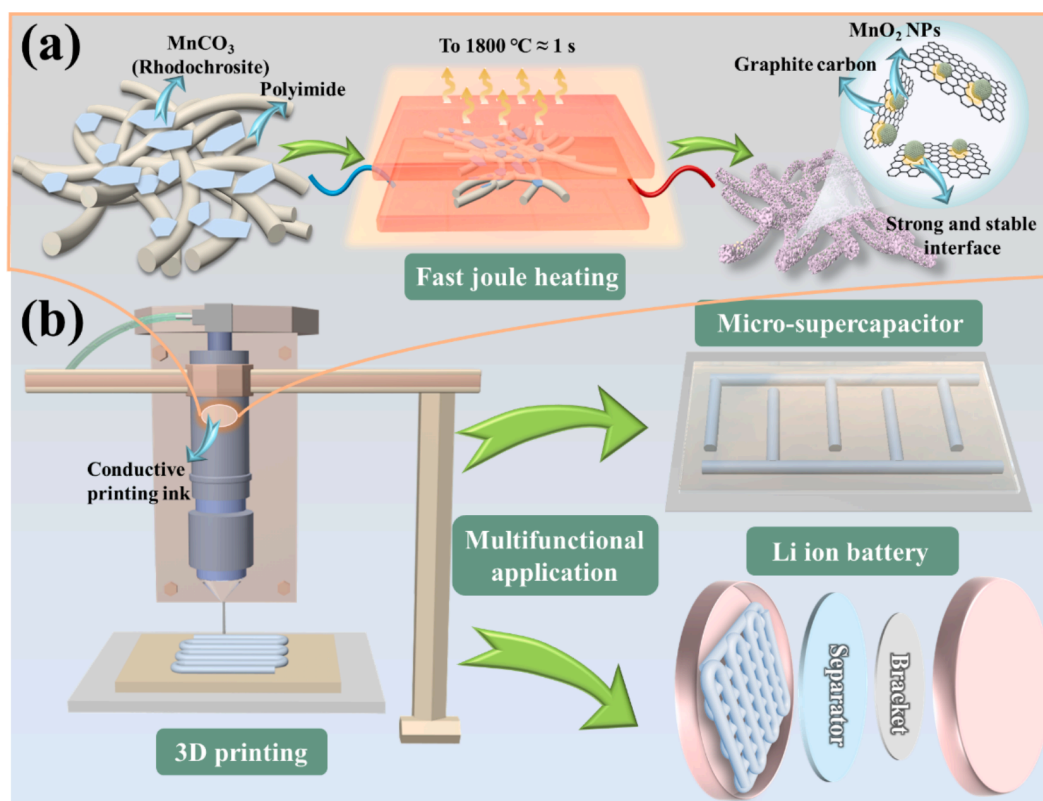


Fig. 1. (a) Schematic diagram of the FJH process for preparing FJH-Mn-C composite material. (b) DIW method for 3D print electrode process and applications.

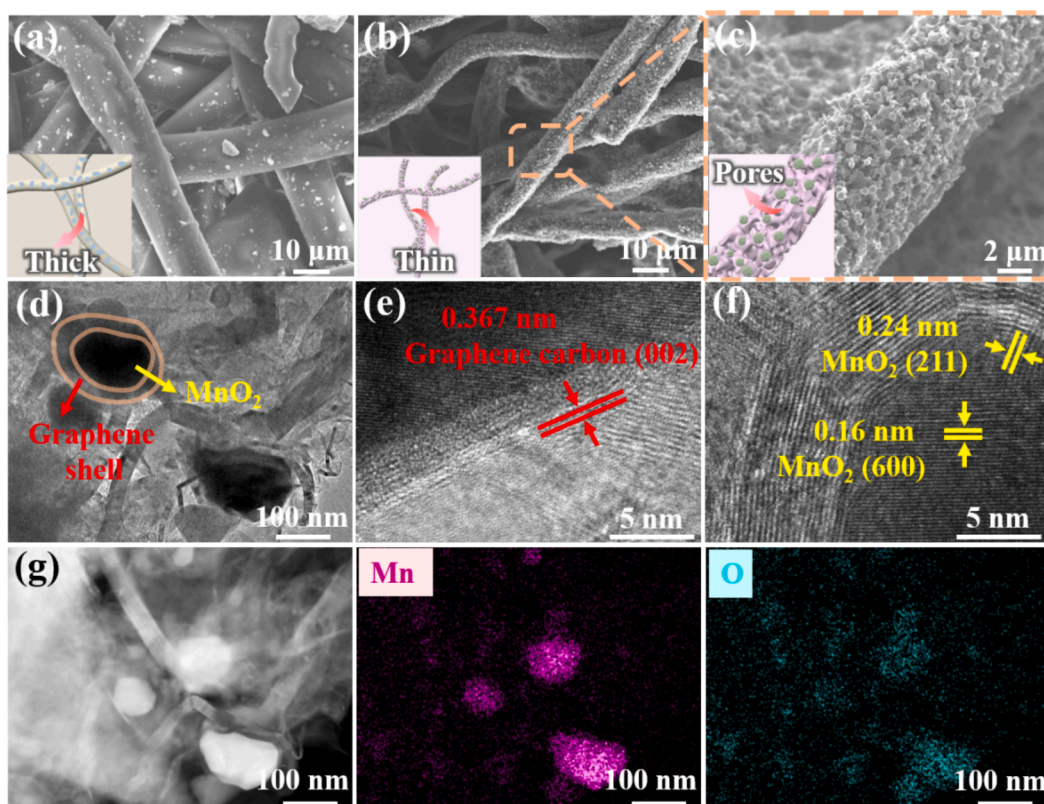


Fig. 2. (a) SEM images of rhodochrosite loaded PI paper. (b-c) Low and high magnified SEM images of FJH-Mn-C-1800. (d) TEM image of FJH-Mn-C-1800. (e-f) HRTEM image of FJH-Mn-C-1800. (g) HAADF-STEM images of FJH-Mn-C-1800.

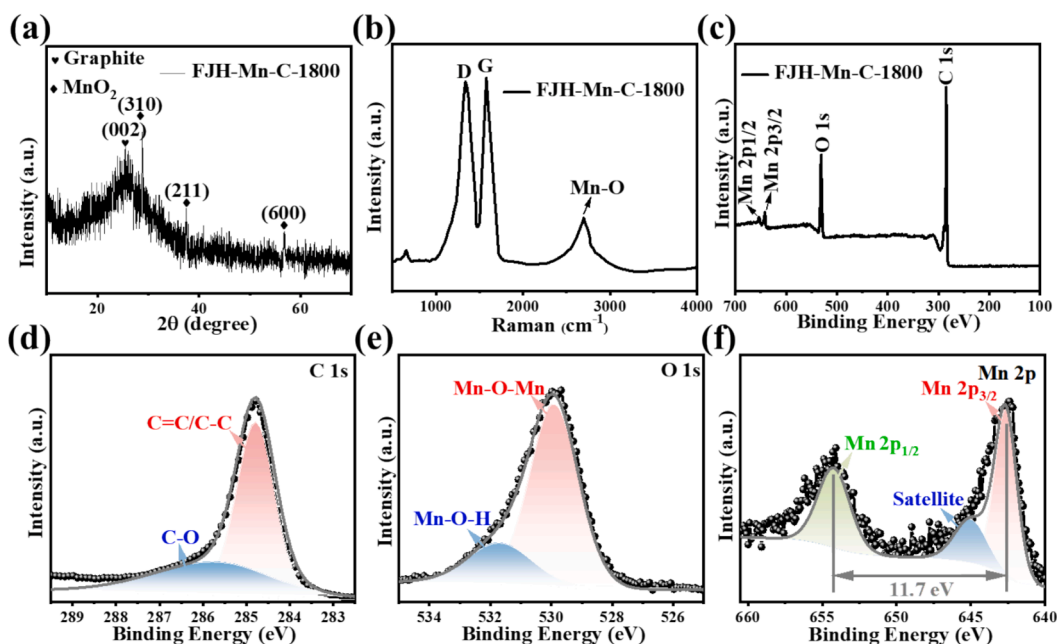


Fig. 3. (a) XRD pattern of FJH-Mn-C-1800. (b) Raman spectra of FJH-Mn-C-1800. (c) XPS spectra of FJH-Mn-C-1800. (d-f) High-resolution XPS spectra of C 1 s, O 1 s, and Mn 2p, respectively.

electrodeposition [24] or wet-chemical techniques [19,25]. While this method allows for precise control over the scaffold structure, it comes with limitations. Since the electroactive nanomaterials are typically deposited only on the surface of the scaffold, the overall material utilization is inefficient, and the limited interface between the conductive scaffold and the electroactive materials can lead to poor charge transfer kinetics. The second approach integrates the conductive materials and electroactive nanomaterials directly into printable ink, which is then used to fabricate the electrode via direct ink writing (DIW) [26]. While this method ensures the uniform distribution of electroactive materials throughout the electrode structure, it also introduces certain drawbacks. The ink formulation often requires the addition of insulating polymer binders, and the intense mixing or grinding processes during ink preparation can disrupt the interaction between the conductive scaffold and electroactive nanomaterials. This can hinder charge transfer efficiency at the interfaces, compromising the electrode's electrochemical performance.

To address these limitations, it is crucial to ensure strong, stable anchoring between conductive scaffolds and electroactive nanomaterials prior to ink formulation. Traditional wet-chemical methods, which rely on a bottom-up approach to grow electroactive materials directly on the conductive matrix, can provide such riveted structures [27,28]. However, these techniques often involve multiple steps, consume large amounts of solvents and chemicals. Moreover, the prolonged processing times and low scalability of wet-chemical methods further limit their practicality for large-scale production. In response to these challenges, extreme nanofabrication methods, such as laser ablation [29–32] and flash joule heating (FJH) [33,34], have gained attention. These methods create non-equilibrium, high-temperature, and high-pressure conditions that enable rapid synthesis of nanomaterials with unique properties. Temperatures exceeding 3000 K can be achieved in microseconds [35], allowing for the formation of riveted structures between conductive scaffolds and electroactive nanomaterials. The rapid synthesis not only minimizes energy consumption and chemical waste but also leads to nanocomposites with high porosity and excellent electrochemical properties. These extreme fabrication techniques are especially suited for the preparation of conductive inks for 3D printing, as they ensure that the nanomaterials are well-integrated and highly functional.

In the present study, we demonstrate the use of FJH method to synthesize MnO_2 /carbon composites to 3D-printed electrode for energy storage applications. MnO_2 was chosen as a typical electrochemically active material due to its high theoretical capacity [36] and pseudocapacitive behavior [37]. The FJH process can achieve extreme reaction conditions of heating to 1800 °C in ≈ 1 s (Fig. 1a, Fig. S1 and Movie. S1), which transforming rhodochrosite/polyimide composite into hierarchically porous MnO_2 /Carbon composites. This composite was subsequently formulated into ink and used to print 3D-structured electrodes (Fig. 1b) for SCs and LIBs. Our results show that the extreme conditions of the FJH method led to a MnO_2 /carbon composite with stronger interfacial interaction between MnO_2 and high porosity carbon (Fig. S2), which contributed to the excellent electrochemical performance of the printed electrodes. The 3D-structured porous electrodes exhibited superior energy storage capabilities compared to conventional bulk electrodes, demonstrating their potential for use in next-generation energy storage devices.

2. Results and discussions

The fabrication of the MnO_2 /carbon composite begins with the FJH treatment of a precursor mixture composed of natural rhodochrosite and polyimide (PI) paper (Fig. 2a). This precursor formulation, derived from our previous work [38], utilizes rhodochrosite as a natural manganese source to generate MnO_2 nanoparticles (NPs). Compared with Mn-containing chemical reagents, rhodochrosite provides notable advantages, including abundant reserves, low cost, and environmental friendliness. In addition, the use of rhodochrosite is also of certain significance for high-value mineral utilization. The PI paper, composed of 17–20 μm PI fibers, is utilized as the carbon source to create a porous carbon matrix. The FJH process involves sandwiching the precursor between two conductive carbon paper electrodes, through which a high electrical current is applied, inducing a rapid temperature rise to approximately 1800 °C within ≈ 1 s (Movie. S1). The resulting composite, referred to as FJH-Mn-C-1800, exhibits a unique combination of MnO_2 NPs and porous carbon fibers (8–10 μm) (Fig. 2b-c), formed by the simultaneous carbonization of PI and the explosive decomposition of rhodochrosite under transient high-temperature conditions. Rapid heating during the FJH treatment plays a pivotal role in the

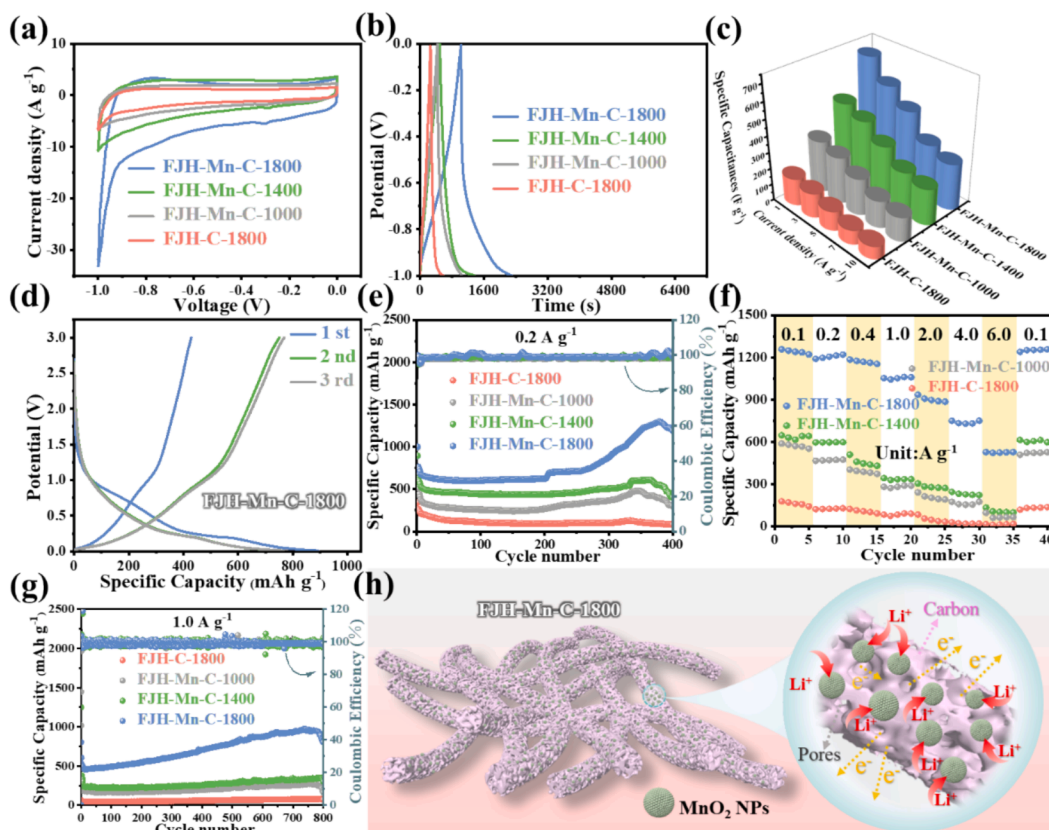


Fig. 4. (a) CV curves of FJH-C-1800 and FJH-Mn-C-X (X = 1000, 1400 and 1800) SCs at a scan rate of 70 mV s⁻¹. (b) Galvanostatic charge-discharge curves of FJH-C-1800 and FJH-Mn-C-X (X = 1000, 1400 and 1800) SCs at a current density of 1 A g⁻¹. (c) Specific capacitance of FJH-C-1800 and FJH-Mn-C-X (X = 1000, 1400 and 1800) SCs. (d) GCD curves of FJH-Mn-C-1800 LIB at different cycles of 0.2 A g⁻¹. (e) Cycling performance of FJH-C-1800 and FJH-Mn-C-X (X = 1000, 1400 and 1800) LIBs with respect to capacity and coulombic efficiency at a current density of 0.2 A g⁻¹. (f) Rate performance from 0.1 A g⁻¹ to 6.0 A g⁻¹ of FJH-C-1800 and FJH-Mn-C-X (X = 1000, 1400 and 1800) LIBs with respect to capacity and coulombic efficiency at a current density of 1.0 A g⁻¹. (g) Cycling performance of FJH-C-1800 and FJH-Mn-C-X (X = 1000, 1400 and 1800) LIBs with respect to capacity and coulombic efficiency at a current density of 1.0 A g⁻¹. (h) Schematic diagram of Li⁺ storage for FJH-Mn-C-1800.

morphological transformation of the precursor materials. The extreme temperature causes micro-sized rhodochrosite particles to disintegrate explosively into uniform MnO₂ NPs, while PI fibers are carbonized into porous carbon fibers, as observed in the scanning electron microscopy (SEM) images (Fig. 2b). The volatile organic compounds within the polyimide matrix evaporate quickly, leaving voids that contribute to the porous nature of the carbon fibers (Fig. 2c). This porous architecture is critical for energy storage applications, as it increases the accessible surface area for electrochemical reactions. It also enhances ion diffusion and promotes efficient electrolyte penetration [39], which are essential for optimizing the performance of Micro-supercapacitors (MSCs) and LIBs.

To further investigate the microstructure of FJH-Mn-C-1800, transmission electron microscopy (TEM) and high-resolution transmission electron microscopy (HRTEM) were employed. TEM images reveal that MnO₂ NPs are well-dispersed and anchored within the carbon matrix. The simultaneous formation of MnO₂ and the carbon matrix during FJH treatment not only facilitates strong attachment of MnO₂ onto the carbon fibers but also results in MnO₂ NPs potentially being enveloped by carbon layers (Fig. 2d). This encapsulation provides structural stability, ensuring that the MnO₂ NPs remain firmly anchored within the carbon matrix during subsequent mechanical processing, such as ink preparation [27,36,38]. Furthermore, the transient high-pressure conditions generated during the FJH process strengthen the junctions between MnO₂ and the carbon matrix, which is crucial for efficient charge transfer in energy storage devices. The robustness of the MnO₂ anchoring was verified by grinding the FJH-Mn-C-1800 composite into a fine powder for ink preparation. Despite the mechanical disruption,

which broke the long carbon fibers into shorter fragments, the MnO₂ NPs remained securely attached to the porous carbon matrix (Fig. S2). This highlights the strong and stable interface between the two components, a critical factor in ensuring long-term electrode performance by preventing detachment or agglomeration of active materials during cycling in energy storage applications [40,41]. The HRTEM analysis (Fig. 2e-f) shows that the lattice spacing of 0.367 nm corresponds to the (002) plane of graphite; the lattice spacings of 0.24 nm and 0.16 nm correspond to the (211) and (600) planes of MnO₂, respectively [38]. The elemental distribution as shown in Fig. 2g visually confirms the uniform distribution of MnO₂ in the carbon fibers. Further characterization of the FJH-Mn-C-1800 was conducted using X-ray diffraction (XRD), Raman spectra, and X-ray photoelectron spectroscopy (XPS). The XRD pattern (Fig. 3a) displayed a prominent diffraction peak at 2θ = 26°, corresponding to the (002) plane of graphitic carbon derived from the polyimide paper. Additional peaks at 2θ = 28.5°, 37.5°, and 56.7° were observed, attributed to characteristic MnO₂ phases [42]. These findings confirm the coexistence of carbon and MnO₂ within the composite material. Raman spectra (Fig. 3b and Fig. S3) further supported these results, with the carbon structure exhibiting characteristic D and G peaks at 1372 cm⁻¹ and 1592 cm⁻¹, respectively, corresponding to defects and sp²-hybridized carbon vibrations in the hexagonal lattice [43]. A broad 2D peak at 2697 cm⁻¹ confirmed the presence of crystalline graphitic domains, while a distinct peak at ~ 650 cm⁻¹ corresponded to the Mn-O bond in MnO₂, indicating successful incorporation of MnO₂ into the carbon matrix [38]. XPS analysis provided additional confirmation of the composite's composition. The full XPS spectra (Fig. 3c) revealed the presence of carbon (C), oxygen (O), and

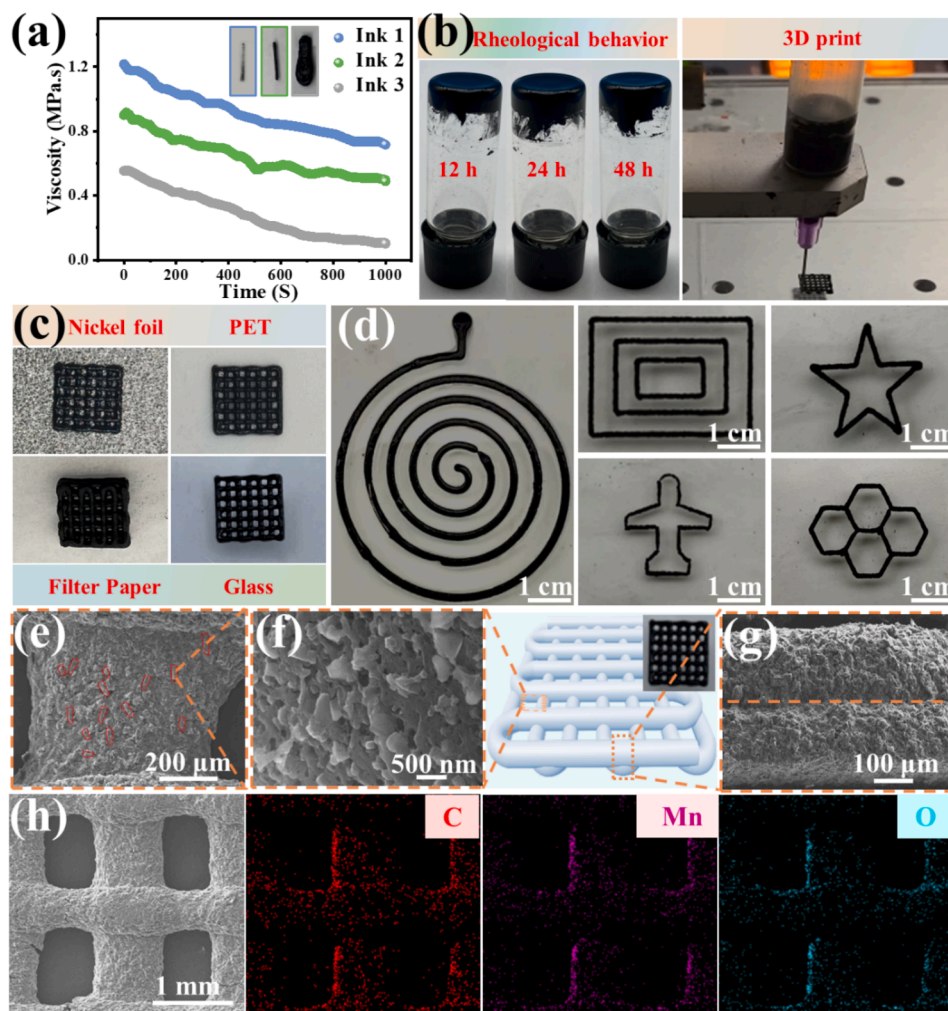


Fig. 5. (a) Rheological behavior of the inks during the extrusion-based 3D printing process. (b) The self-supporting properties and actual printing process of ink 2. (c) Printing microlattice on different substrates. (d) Optical images of various patterns printed by 3D printing. (e-f) Top SEM images of the microlattice. (g) Cross-section SEM images of the microlattice. (h) Top SEM-EDS mapping of microlattice with C, Mn, and O elements.

manganese (Mn), consistent with the expected material composition. The high-resolution C 1 s spectra (Fig. 3d) showed peaks at 285.8 eV and 284.8 eV, corresponding to C-O and C = C/C-C bonds, respectively. The O 1 s spectra (Fig. 3e) exhibited peaks at 529.8 eV and 532.1 eV, indicating Mn-O-H and Mn-O-Mn bonds [44]. The Mn 2p spectra (Fig. 3f) displayed characteristic peaks at 642.5 eV and 654.2 eV, with a peak separation of 11.7 eV, confirming the Mn⁴⁺ oxidation state in MnO₂ [45]. These results collectively demonstrate that the FJH method successfully synthesized MnO₂/carbon composites with well-integrated MnO₂ NPs anchored onto the carbon matrix.

Before employing the FJH-Mn-C composite for 3D printing, its electrochemical performance as a SC was evaluated using a three-electrode system. To assess the influence of the FJH processing temperature, FJH-Mn-C composites were prepared at varying temperatures of 1000 °C, 1400 °C, and 1800 °C, referred to as FJH-Mn-C-1000, FJH-Mn-C-1400, and FJH-Mn-C-1800, respectively. A pure carbon sample derived from polyimide paper processed at 1800 °C served as a control. The cyclic voltammetry (CV) (Fig. 4a and S4) and galvanostatic charge-discharge (GCD) (Fig. 4b and S5) curves demonstrated that the MnO₂/C composites exhibited a larger CV area and longer discharge times compared to the pure carbon sample, indicating a significant pseudocapacitance contribution from MnO₂. Notably, a redox peak at 0.39 V was observed, corresponding to the MnO₂ energy storage mechanism [46]. Among the various composites, FJH-Mn-C-1800 exhibited the best electrochemical performance, as reflected in both

CV and GCD curves. Specific capacitance values calculated (Fig. 4c) from the GCD curves further confirmed the superior performance of FJH-Mn-C-1800 (692.3 F g⁻¹@1 A g⁻¹) compared to FJH-Mn-C-1400 (473.7 F g⁻¹@1 A g⁻¹) and FJH-Mn-C-1000 (315.8 F g⁻¹@1 A g⁻¹). The superior performance of FJH-Mn-C-1800 compared to FJH-Mn-C-1400 and FJH-Mn-C-1000 is attributed to the extreme reaction conditions at 1800 °C, including extreme high temperature, high pressure, and non-equilibrium [47]. This process resulted in the formation of a more porous carbon matrix and smaller MnO₂ NPs in FJH-Mn-C-1800 (Fig. 2c and Fig. S6). These features also contribute to higher specific surface areas (Fig. S7a) and pore volumes (Fig. S7b), which facilitating improved mass, ion, and charge exchange, which facilitating improved mass, ion, and charge exchange. Additionally, the higher temperature enhances the crystallinity of the carbon matrix, as shown in the XRD patterns (Fig. S8), and improves conductivity, reflected in reduced series resistance (Fig. S9), thus enhancing electron transport rates.

The superior electrochemical performance of FJH-Mn-C-1800 also extended to its use as an anode material in LIB. Within a voltage window of 0.01–3.0 V, the initial discharge and charge capacities of FJH-Mn-C-1800 were 891.5 mAh g⁻¹ and 428.6 mAh g⁻¹ (Fig. 4d), respectively, significantly higher than those of FJH-Mn-C-1400 (Fig. S10a) and FJH-Mn-C-1000 (Fig. S10b). The cycling performance (Fig. 4e) showed that the capacity of FJH-Mn-C-1800 increased to 1190.9 mAh g⁻¹ at 0.2 A g⁻¹ after 400 cycles, with a coulombic efficiency of 99.4 %. Furthermore, its rate performance demonstrated the highest capacity retention across all

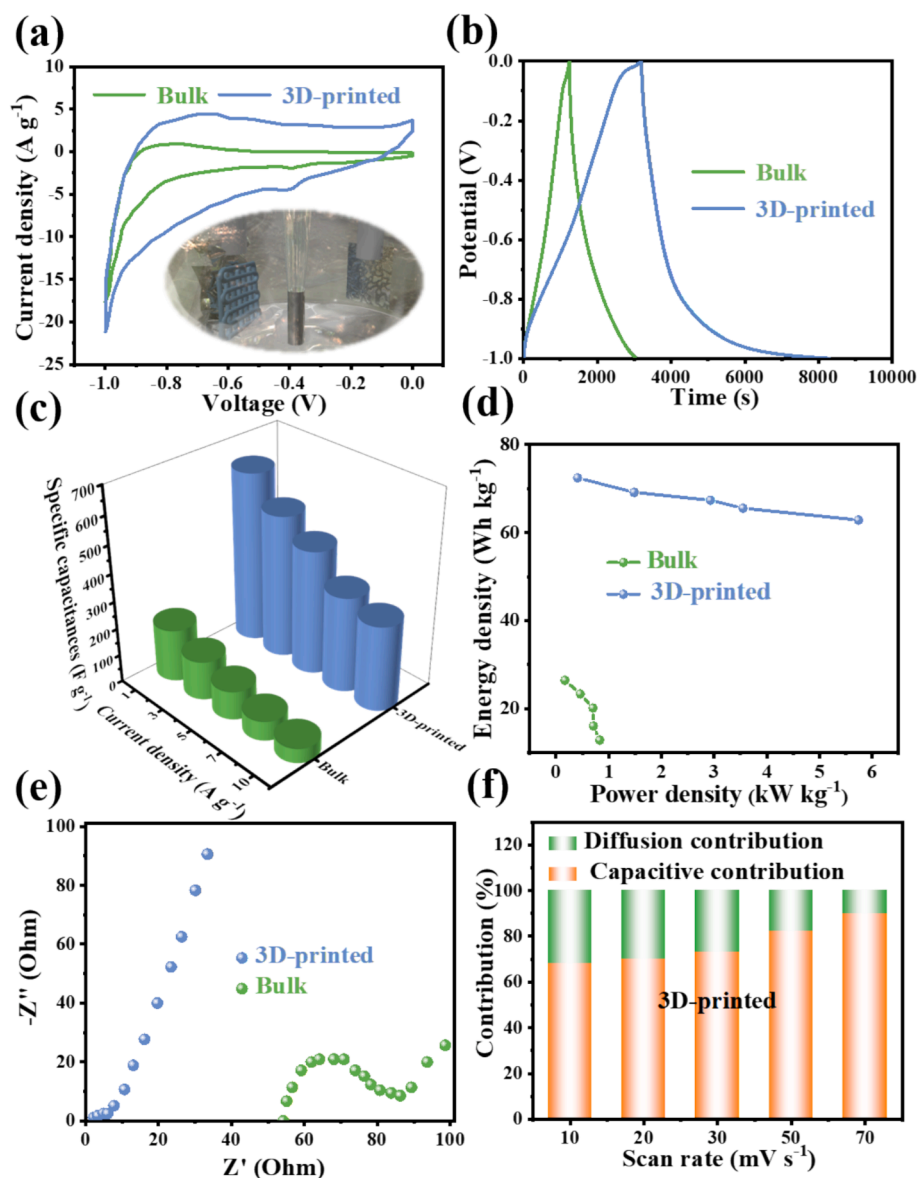


Fig. 6. (a) CV curves of bulk and 3D-printed SCs at a scan rate of 70 mV s^{-1} . (b) GCD curves of bulk and 3D-printed SCs at a current density of 1 A g^{-1} . (c) Specific capacitance of bulk and 3D-printed SCs at different current densities ($1\text{--}10 \text{ A g}^{-1}$). (d) Ragone diagrams of bulk and 3D-printed SCs. (e) Nyquist plots of bulk and 3D-printed SCs. (f) Contribution percentages of the capacitive and diffusion-controlled process at different scan rates ($10\text{--}70 \text{ mV s}^{-1}$) of 3D-printed SCs.

current densities, with excellent recovery. At 1.0 A g^{-1} , FJH-Mn-C-1800 maintained the highest capacity (Fig. 4f). Moreover, at 1.0 A g^{-1} , FJH-Mn-C-1800 LIB also demonstrates remarkable cycling performance, maintaining a capacity of 801.2 mAh g^{-1} after 800 cycles (Fig. 4g), which is better than most reported MnO_2/C anodes [48–50]. Compared with FJH-Mn-C-1400 and FJH-Mn-C-1000 LIBs, FJH-Mn-C-1800 LIB shows superior electrochemical performance. This can be due to its more hierarchical porous carbon fibers and uniformly distributed MnO_2 NPs (Fig. 2c) significantly improving the pathways for ion and electron transport (Fig. 4h), which enhances reaction kinetics. Electrochemical impedance spectroscopy (EIS) results support this point in the following two aspects: As shown in Fig. S11 and Table S1, compared to FJH-Mn-C-1400 (134.5Ω) and FJH-Mn-C-1000 LIBs (138.2Ω), FJH-Mn-C-1800 LIB (112.2Ω) has a lower charge transfer resistance (Rct), indicating faster charge transfer behavior [51,52]; Further analysis of Z' and $\omega^{-1/2}$ using eq. (S9) was conducted to determine the value of warburg impedance factors (δ). The δ value of FJH-Mn-C-1800 is lower than FJH-Mn-C-1400 and FJH-Mn-C-1000, indicating that FJH-Mn-C-1800 exhibits faster Li^+ diffusion capacity [53].

In subsequent experiments, FJH-Mn-C-1800 was utilized as the active material (120 mg) to prepare 3D printing inks with varying amounts of NMP solvent: 1.0 mL , 1.5 mL , and 2.0 mL , denoted as ink 1, ink 2, and ink 3, respectively. Viscosity measurements (Fig. 5a) demonstrated that all inks exhibited shear-thinning behavior. Among them, ink 2 demonstrated optimal printability. In contrast, ink 1 was excessively viscous, causing nozzle clogging, while ink 3 had too insufficient viscosity, resulting in structural instability. The viscosity of ink 2, ranging from 0.6 to $0.9 \text{ MPa}\cdot\text{s}$, aligns with the typical viscosity range of 3D printing inks reported in previous studies [54]. Ink 2 displayed excellent self-supporting properties and good fluidity (Fig. 5b), successfully printing complex structures on substrates such as glass, PET, nickel foam and paper (Fig. 5c and Movie. S2). It allowed for the formation of intricate patterns, including microlattices and hexagonal grids (Fig. 5d). SEM analysis of the 3D-printed microlattice revealed an orderly, porous structure with uniformly dispersed FJH-Mn-C-1800 short fragment (Fig. 5e–f). The microlattice cross-section revealed a layer thickness of approximately $170 \mu\text{m}$ (Fig. 5g). Energy-dispersive spectroscopy (EDS) mapping analysis showed a uniform distribution of

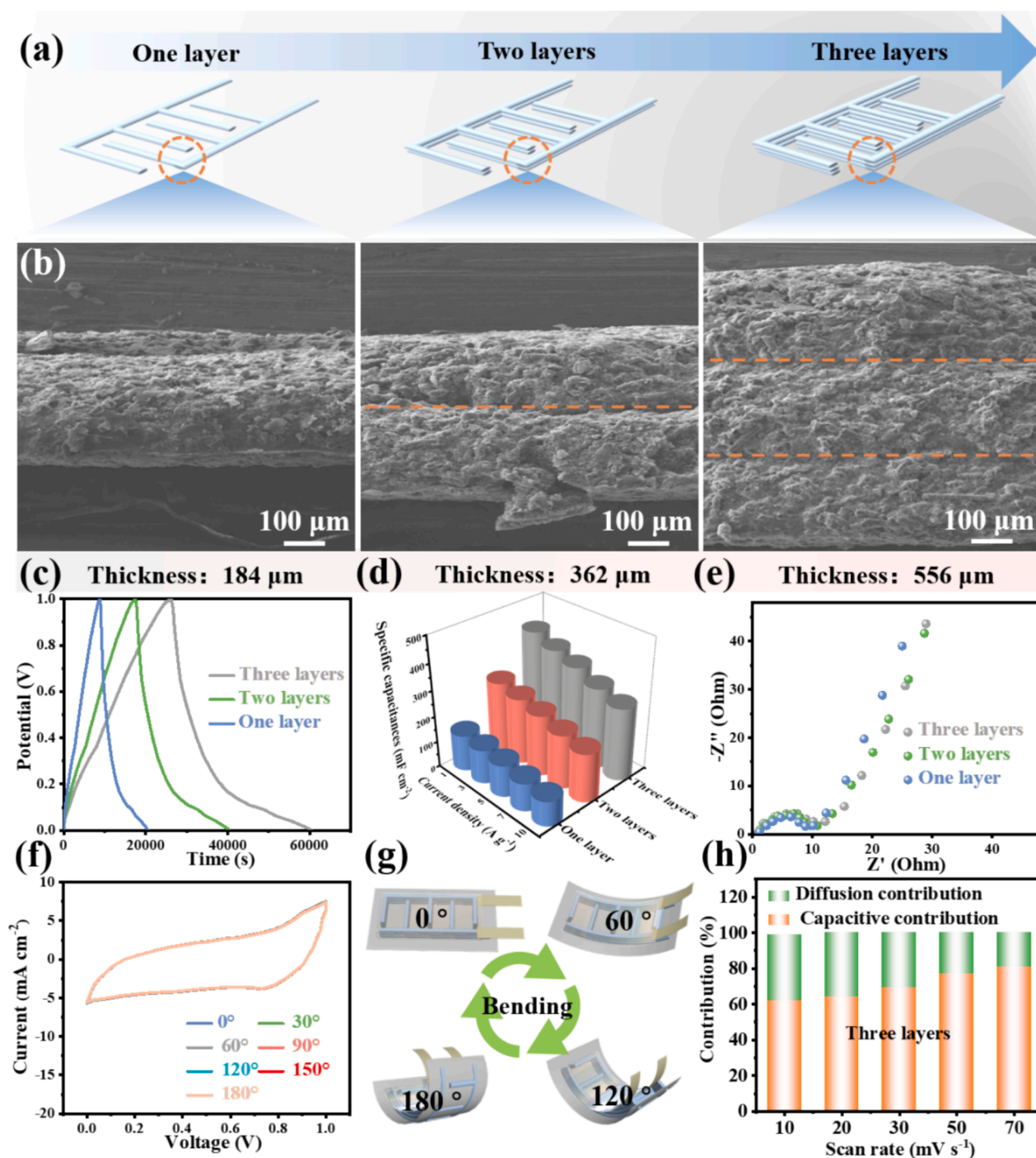


Fig. 7. (a–b) Cross-section view of 1 layer, 2 layers and 3 layers 3D-printed MSCs. (c) GCD curves of 1 layer, 2 layers and 3 layers 3D-printed MSCs at a current density of 1 A g⁻¹ (d) Area specific capacitance of 1 layer, 2 layers and 3 layers 3D-printed MSCs at different current densities (1–10 A g⁻¹). (e) Nyquist plots of 1 layer, 2 layers and 3 layers 3D-printed MSCs. (f–g) CV curves and capacitance retention of 3 layers 3D-printed MSC under bending angles from 0° to 180° at 70 mV s⁻¹. (h) Contribution percentages of the capacitive and diffusion-controlled process at different scan rates (10–70 mV s⁻¹) of 3 layers 3D-printed MSC.

C, O, and Mn elements throughout the structure, confirming the successful integration of MnO₂ NPs (Fig. 5h and S12).

The microlattice electrode was then fabricated on nickel foil for use in a three-electrode supercapacitor (3D-printed SC). A conventional electrode prepared via bulk coating served as a reference (bulk SC). CV (Fig. 6a and S13) and GCD (Fig. 6b and S14) tests showed that the 3D-printed SC had a significantly larger CV curve area and longer discharge time compared to the bulk SC, suggesting much higher capacitance. At 10 A g⁻¹, the specific capacitance of the 3D-printed SC reached 309.6 F g⁻¹, which is 5.8 times higher than the bulk SC (Fig. 6c).

Additionally, the 3D-printed SC exhibited an energy density of 72.5 Wh kg⁻¹, 3.1 times that of the bulk SC (Fig. 6d). EIS results (Fig. 6e) indicated lower series resistance and improved ion transfer efficiency for the 3D-printed SC, attributed to the hierarchical pore structure that enhances capacitance and ion diffusion. Further analysis of the energy storage mechanisms (Fig. 6f and S15–16) showed that the capacitance-controlled process dominated in the 3D-printed SC, accounting for 90 % of the energy storage at a scan rate of 70 mV s⁻¹, compared to only 62 % in the bulk SC (Fig. S16). This indicates faster charge transfer kinetics in the 3D-printed SC.

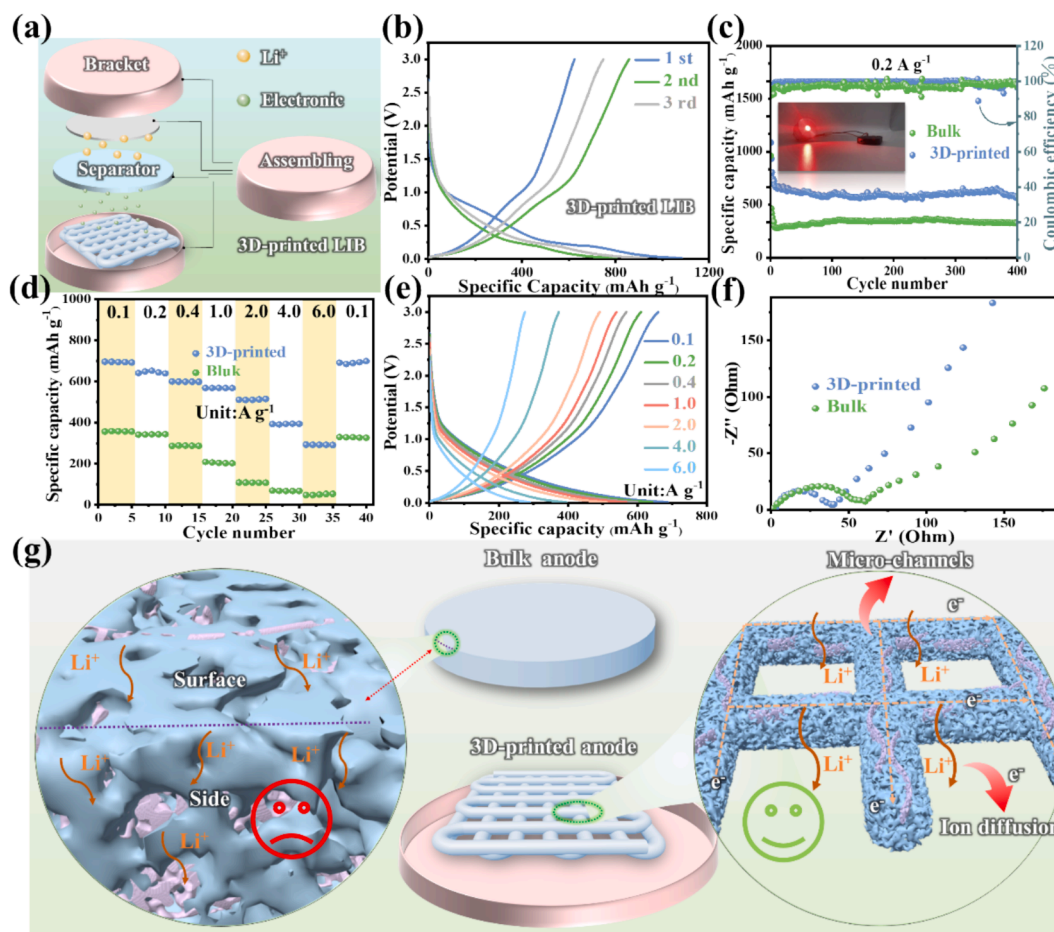


Fig. 8. (a) Schematic diagram of the construction of 3D-printed LIB. (b) GCD curves of 3D-printed LIB at different cycles of 0.2 A g⁻¹. (c) Cycling performance of bulk and 3D-printed LIBs with respect to capacity and coulombic efficiency at a current density of 0.2 A g⁻¹. (d-e) Rate performance from 0.1 A g⁻¹ to 6.0 A g⁻¹ of bulk and 3D-printed LIBs. (f) Nyquist plots of bulk and 3D-printed LIBs. (g) Schematic diagram of Li⁺ storage advantages in 3D-printed LIB.

To explore the scalability of our approach, one-layer, two-layers, and three-layers interdigitated electrodes were printed on PET substrates to create MSCs, which were subsequently combined with gel electrolytes. SEM analysis showed that the electrode thicknesses were proportional to the number of printed layers, with the one-layer, two-layers, and three-layers MSCs measuring 184 μm , 362 μm , and 556 μm , respectively (Fig. 7a-b). CV (Fig. S17) and GCD (Fig. 7c and S18) tests revealed that the three-layers MSC exhibited the highest specific capacitance (Fig. 7d), as demonstrated by the larger integrated CV curve area and longer discharge times. The three-layers MSC had a specific area capacitance of 411.3 mF cm⁻² at 1.0 A g⁻¹, which was three times higher than that of the one-layer MSC (139.5 mF cm⁻²). Even at a high current density of 10.0 A g⁻¹, the three-layers MSC retained a specific area capacitance of 279 mF cm⁻², surpassing most reported MSCs of this type (Table S2). The EIS results (Fig. 7e) indicated that the charge transport dynamics were similar across all MSCs, regardless of the number of printed layers, demonstrating consistent ion and electron transport. Furthermore, the three-layers MSC exhibited excellent cycling stability, retaining 90 % of its capacitance after 1000 charge-discharge cycles (Fig. S19). This stability is attributed to the uniform distribution of FJH-Mn-C-1800 composite by 3D printing, which facilitates efficient contact between electrolyte ions and active sites. Flexibility tests (Fig. 7f-g) showed that the three-layers MSC maintained nearly unchanged CV curves under varying bending angles. There was only a 3 % decrease in capacitance at a 180° bending angle, indicating minimal impact from mechanical deformation. Energy storage mechanism analysis (Fig. 7h and S20-21) showed that capacitance control was the dominant mechanism in all

MSCs, accounting for over 80 % of the total energy storage at higher scan rates. This suggests that ion and electron transport remained efficient even with increased electrode thickness.

Finally, LIBs were assembled using both 3D-printed microlattice electrodes and traditional bulk electrodes with comparable active material loadings, referred to as 3D-printed LIB and bulk LIB, respectively (Fig. 8a). The electrochemical performance of these systems was thoroughly examined, revealing significant advantages for the 3D-printed electrodes. According to the GCD curves in Fig. 8b and Fig. S22, the initial discharge capacity of 3D-printed LIB reaches 1082 mAh g⁻¹ at 0.2 A g⁻¹, significantly outperforming the bulk LIB (709.9 mAh g⁻¹). As shown in Fig. 8c, after 400 cycles at 0.2 A g⁻¹, the 3D-printed LIB retained a capacity of 570.9 mAh g⁻¹, compared to only 325.8 mAh g⁻¹ for the bulk LIB. The capacity of the 3D-printed LIB initially decreased and then increased during cycling, attributed to the formation of a solid-electrolyte interphase (SEI) layer [55-57] and the activation of MnO₂ NPs in the electrode [38]. Moreover, the feasibility of practical applications for 3D-printed LIB was demonstrated, as shown in Fig. 8c (inset), where the device successfully powered a red LED. Even at a high current density of 1 A g⁻¹, the 3D-printed LIB achieved a maximum capacity of 610.7 mAh g⁻¹ (Fig. S23), which is comparable to previously reported MnO₂/C-based LIBs (Table S3). After 800 cycles, the 3D-printed LIB retained a capacity of 485.7 mAh g⁻¹, far exceeding the bulk LIB, which dropped to 112.3 mAh g⁻¹. Rate performance tests (Fig. 8d-e) at current densities ranging from 0.1 A g⁻¹ to 6.0 A g⁻¹ demonstrated the superior capacity of the 3D-printed LIB. Its capacities were 695.6 mAh g⁻¹, 640.7 mAh g⁻¹, 599.2 mAh g⁻¹, 568.2 mAh g⁻¹, 510.6 mAh g⁻¹, 390.7 mAh

g^{-1} , and 291.8 mAh g^{-1} , significantly better than the bulk LIB, which recorded 357.7 mAh g^{-1} , 342.5 mAh g^{-1} , 287.7 mAh g^{-1} , 203.9 mAh g^{-1} , 108 mAh g^{-1} , 67.9 mAh g^{-1} , and 50.1 mAh g^{-1} . When the current density returned to 0.1 A g^{-1} , the capacity of the 3D-printed LIB recovered to 691 mAh g^{-1} , demonstrating excellent reversibility. To understand the improved performance of the 3D-printed LIB, EIS was conducted (Fig. 8f). The Nyquist plots show that the 3D-printed LIB exhibits significantly lower series resistance (R_s) than the bulk LIB, indicating better ion conductivity. Compared to bulk LIB, the 3D-printed LIB exhibits a higher slope in the low-frequency region, indicating stronger reaction kinetics. This improvement is likely attributed to the microlattice structure, which enhances the efficiency of ion and electron transport. In summary, the superior electrochemical performance of the 3D-printed LIB can be attributed to its three-dimensional hierarchical porous architecture (Fig. 8g), which facilitates electrolyte penetration, accelerates ion/electron transport, and improves reaction kinetics. Furthermore, the uniform distribution of FJH-Mn-C-1800 within the microlattice electrode ensures optimal contact with the electrolyte, contributing to the excellent rate capability and long-term cycling stability of the 3D-printed LIB.

3. Conclusion

In summary, we employed the carbothermal shock method to rapidly synthesize MnO_2 /carbon composites as electrochemically active materials for 3D-printed electrodes in energy storage devices. The extreme reaction conditions, reaching 1800°C within 1 s, enabled the transformation of rhodochrosite into MnO_2 NPs anchored on porous carbon fibers derived from PI. This unique structure enhanced interfacial interactions, leading to superior electrochemical performance. Using a scalable direct ink writing technique, we fabricated 3D-printed electrodes with hierarchical porous architectures, achieving a high specific capacitance of 411.3 mF cm^{-2} at 1.0 A g^{-1} for MSCs and exceptional flexibility under mechanical deformation. For LIBs, the 3D-printed porous electrodes exhibited a stable capacity of 570.9 mAh g^{-1} after 400 cycles with a 97.8 % coulombic efficiency, significantly outperforming traditional bulk electrodes. This work highlights the potential of combining FJH method synthesis and 3D printing to develop advanced, high-performance materials for next-generation energy storage applications.

CRedit authorship contribution statement

Jun Cao: Writing – original draft. **Chunjie Yan:** Data curation. **Qi Sun:** Data curation. **Xiaoyan Zhu:** Investigation. **Sen Zhou:** Project administration. **Ziming Song:** Supervision. **Zhigang Wang:** Investigation. **Heng Deng:** Writing – review & editing.

Declaration of competing interest

The authors declare that they have no known competing financial interests or personal relationships that could have appeared to influence the work reported in this paper.

Acknowledgments

This work was supported by the National Natural Science Foundation of China (Grant No. 52303163), Guangdong Basic and Applied Basic Research Foundation (Grant No. 2022A1515110026), “CUG Scholar” Scientific Research Funds at China University of Geosciences (Wuhan) (Project No.2022010) and Fundamental Research Funds for the Central Universities, China University of Geosciences (Wuhan) (No. CUG240613).

Appendix A. Supplementary data

Supplementary data to this article can be found online at <https://doi.org/10.1016/j.cej.2025.159723>.

Data availability

Data will be made available on request.

References

- [1] S. Deshmukh, S. Kunuku, P. Jakobczyk, A. Olejnik, C.H. Chen, H. Niu, B. Yang, N. Yang, R. Bogdanowicz, Diamond-Based Supercapacitors with Ultrahigh Cyclic Stability Through Dual-Phase MnO_2 -Graphitic Transformation Induced by High-Dose Mn-Ion Implantation, *Adv. Funct. Mater.* 34 (8) (2024) 2308617.
- [2] P. Lu, D. Xue, H. Yang, Y. Liu, Supercapacitor and nanoscale research towards electrochemical energy storage, *Int. J. Smart Nano Mater.* 4 (1) (2013) 2–26.
- [3] X. Yuan, Z. Ma, S. Jian, H. Ma, Y. Lai, S. Deng, X. Tian, C.-P. Wong, F. Xia, Y. Dong, Mesoporous nitrogen-doped carbon MnO_2 multichannel nanotubes with high performance for Li-ion batteries, *Nano Energy* 97 (2022) 107235.
- [4] F. Degen, M. Winter, D. Bendig, J. Tübke, Energy consumption of current and future production of lithium-ion and post lithium-ion battery cells, *Nat. Energy* 8 (11) (2023) 1284–1295.
- [5] R. Qiu, D. Ma, H. Zheng, M. Liu, J. Cai, W. Yan, J. Zhang, Performance degradation mechanisms and mitigation strategies of hard carbon anode and solid electrolyte interface for sodium-ion battery, *Nano Energy* 109920 (2024).
- [6] H. Zhang, F. Gao, D. Zhang, C. Gao, G. Huang, Z. Zhang, Y. Liu, M. Terrones, J. Wei, Y. Wang, Biomimetic mineralization synergistic combustion activation to construct honeycomb porous carbon anode for sodium-ion batteries, *Carbon* 230 (2024) 119602.
- [7] F. Xiankai, X. Kaixiong, Z. Wei, D. Weina, Z. Hai, C. Liang, C. Han, A novel improvement strategy and a comprehensive mechanism insight for $\alpha\text{-MnO}_2$ energy storage in rechargeable aqueous zinc-ion batteries, *Carbon Energy* (2024) e536.
- [8] W. Lv, Z. Shen, X. Li, J. Meng, W. Yang, F. Ding, X. Ju, F. Ye, Y. Li, X. Lyu, Discovering Cathodic Biocompatibility for Aqueous Zn– MnO_2 Battery: An Integrating Biomass Carbon Strategy, *Nano-Micro Lett.* 16 (1) (2024) 109.
- [9] A.N. Singh, M. Islam, A. Meena, M. Faizan, D. Han, C. Bathula, A. Hajibabaei, R. Anand, K.W. Nam, Unleashing the potential of sodium-ion batteries: current state and future directions for sustainable energy storage, *Adv. Funct. Mater.* 33 (46) (2023) 2304617.
- [10] Q. Wang, P. Zou, L. Ren, S. Wang, Y. Wang, Z. Huang, Z. Hou, Z. Jiang, X. Lu, T. Lu, Ultrathin Composite Li Electrode for High-Performance Li Metal Batteries: A Review from Synthetic Chemistry, *Adv. Funct. Mater.* 33 (18) (2023) 2213648.
- [11] N. Fonseca, S.V. Thummalapalli, S. Jambhulkar, D. Ravichandran, Y. Zhu, D. Patil, V. Thippanna, A. Ramanathan, W. Xu, S. Guo, 3D Printing-Enabled Design and Manufacturing Strategies for Batteries: A Review, *Small* 19 (50) (2023) 2302718.
- [12] X. Hu, Y. Chen, W. Xu, Y. Zhu, D. Kim, Y. Fan, B. Yu, Y. Chen, 3D-Printed Thermoplastic Polyurethane Electrodes for Customizable, Flexible Lithium-Ion Batteries with an Ultra-Long Lifetime, *Small* 19 (34) (2023) 2301604.
- [13] R. Yuan, S. Sun, S. Ling, T. Zhou, H. He, X. Li, C. Zhang, Solvent exchange assisted 3D printing of low tortuosity thick electrode for high areal energy density and power density supercapacitors, *Carbon* 218 (2024) 118737.
- [14] Z. Zhang, K.G. Demir, G.X. Gu, Developments in 4D-printing: a review on current smart materials, technologies, and applications, *Int. J. Smart Nano Mater.* 10 (3) (2019) 205–224.
- [15] S. Mubarak, D. Dhamodharan, H.-S. Byun, Recent advances in 3D printed electrode materials for electrochemical energy storage devices, *J. Energy Chem.* 81 (2023) 272–312.
- [16] S. Huo, L. Sheng, B. Su, W. Xue, L. Wang, H. Xu, X. He, 3D Printing Manufacturing of Lithium Batteries: Prospects and Challenges Toward Practical Applications, *Adv. Mater.* 36 (8) (2024) 2310396.
- [17] H. Ren, X. Yang, Z. Wang, X. Xu, R. Wang, Q. Ge, Y. Xiong, Smart structures with embedded flexible sensors fabricated by fused deposition modeling-based multimaterial 3D printing, *Int. J. Smart Nano Mater.* 13 (3) (2022) 447–464.
- [18] L. Zhang, J. Qin, P. Das, S. Wang, T. Bai, F. Zhou, M. Wu, Z.S. Wu, Electrochemically Exfoliated Graphene Additive-Free Inks for 3D Printing Customizable Monolithic Integrated Micro-Supercapacitors on a Large Scale, *Adv. Mater.* 36 (19) (2024) 2313930.
- [19] Z. Yang, X. Yang, T. Yang, Y. Cao, C. Zhang, Y. Zhang, P. Li, J. Yang, Y. Ma, Q. Li, 3D printing of carbon tile-modulated well-interconnected hierarchically porous pseudocapacitive electrode, *Energy Storage Mater.* 54 (2023) 51–59.
- [20] H. Ye, Y. He, T. You, F. Xu, Advanced MXene/Graphene Oxide/Lignosulfonate Inks for 3D Printing Thick Electrodes with Vertically Aligned Pores to Dually Boost Mass Loading and Areal Capacitance, *Adv. Funct. Mater.* 2413343 (2024).
- [21] D. Lin, S. Chandrasekaran, J.B. Forien, X. Xue, A. Pinongcos, E. Coester, M. A. Worsley, Y. Li, 3D-Printed Graded Electrode with Ultrahigh MnO_2 Loading for Non-Aqueous Electrochemical Energy Storage, *Adv. Energy Mater.* 13 (20) (2023) 2300408.
- [22] H. Zhou, Y. Sun, H. Yang, Y. Tang, Y. Lu, Z. Zhou, S. Cao, S. Zhang, S. Chen, Y. Zhang, Co_3O_4 Quantum Dots Intercalation Liquid-Crystal Ordered-Layered-Structure Optimizing the Performance of 3D-Printing Micro-Supercapacitors, *Adv. Sci.* 10 (33) (2023) 2303636.

- [23] T.C. Doan, B. Muthukutty, H. Yoo, High mass-loading of nickel-cobalt layered double hydroxide on 3D-printed electrode for cathode of asymmetric supercapacitor, *J. Energy Storage* 68 (2023) 107648.
- [24] H. Gao, W. Gao, M. Pumera, 3D-Printed Nanostructured Copper Substrate Boosts the Sodiated Capability and Stability of Antimony Anode for Sodium-Ion Batteries, *Adv. Funct. Mater.* 34 (19) (2024) 2310563.
- [25] B.K. Deka, A. Hazarika, G.-H. Kang, Y.J. Hwang, A.P. Jaiswal, D. Chan Kim, Y.-B. Park, H.W. Park, 3D-printed structural supercapacitor with MXene-N@ Zn-Co selenide nanowire based woven carbon fiber electrodes, *ACS Energy Lett.* 8 (2) (2023) 963–971.
- [26] L. Zeng, S. Ling, D. Du, H. He, X. Li, C. Zhang, Direct Ink Writing 3D Printing for High-Performance Electrochemical Energy Storage Devices: A Minireview, *Adv. Sci.* 10 (32) (2023) 2303716.
- [27] H. Jia, Y. Cai, J. Lin, H. Liang, J. Qi, J. Cao, J. Feng, W. Fei, Heterostructural graphene quantum dot/MnO₂ nanosheets toward high-potential window electrodes for high-performance supercapacitors, *Adv. Sci.* 5 (5) (2018) 1700887.
- [28] H. Jiang, Z. Wang, Q. Yang, M. Hanif, Z. Wang, L. Dong, M. Dong, A novel MnO₂/Ti₃C₂T_x MXene nanocomposite as high performance electrode materials for flexible supercapacitors, *Electrochim. Acta* 290 (2018) 695–703.
- [29] M. Han, Y. Zhu, G. Wang, X. Ding, J. Liu, S. Luo, Full laser irradiation processed Pb-graphene nanocomposite electrodes toward the manufacturing of high-performance supercapacitors, *Carbon* 216 (2024) 118583.
- [30] Y. Gao, Y. Cao, Y. Luo, G. Wang, W. Zhao, X. Ding, S. Luo, Stackable and Deployable Laser-Induced Graphene Layers Toward the Flexible Manufacturing of Smart 3D Honeycombs with Multifunctional Performance, *Adv. Funct. Mater.* 2316533 (2024).
- [31] W. Yang, M. Han, F. Liu, D. Wang, Y. Gao, G. Wang, X. Ding, S. Luo, Structure-Foldable and Performance-Tailorable PI Paper-Based Triboelectric Nanogenerators Processed and Controlled by Laser-Induced Graphene, *Adv. Sci.* 2310017 (2024).
- [32] F. Liu, Y. Gao, G. Wang, D. Wang, Y. Wang, M. He, X. Ding, H. Duan, S. Luo, Laser-Induced Graphene Enabled Additive Manufacturing of Multifunctional 3D Architectures with Freeform Structures, *Adv. Sci.* 10 (4) (2023) 2204990.
- [33] X. Hu, D. Zuo, S. Cheng, S. Chen, Y. Liu, W. Bao, S. Deng, S.J. Harris, J. Wan, Ultrafast materials synthesis and manufacturing techniques for emerging energy and environmental applications, *Chem. Soc. Rev.* 52 (3) (2023) 1103–1128.
- [34] Y. Chen, Z. Liu, Z. Wang, Y. Yi, C. Yan, W. Xu, F. Zhou, Y. Gao, Q. Zhou, C. Zhang, Bioinspired Robust Gas-Permeable On-Skin Electronics: Armor-Designed Nanoporous Flash Graphene Assembly Enhancing Mechanical Resilience, *Adv. Sci.* 2402759 (2024).
- [35] S. Dou, J. Xu, X. Cui, W. Liu, Z. Zhang, Y. Deng, W. Hu, Y. Chen, High-temperature shock enabled nanomanufacturing for energy-related applications, *Adv. Energy Mater.* 10 (33) (2020) 2001331.
- [36] X. Cheng, X. Tian, S. Liao, Q. Wang, Q. Wei, Wet spinning for high-performance fiber supercapacitor based on Fe-doped MnO₂ and graphene, *Carbon* 230 (2024) 119572.
- [37] L. Deng, Z. Wang, H. Cui, Y. Guo, Z. Ye, H. Li, X. Zhang, P. Jia, Q. Zhang, L. Zhang, Mechanistic Understanding of the Underlying Energy Storage Mechanism of α -MnO₂-based Pseudo-Supercapacitors, *Adv. Mater.* 2408476.
- [38] J. Cao, C. Yan, Z. Chai, Z. Wang, M. Du, G. Li, H. Wang, H. Deng, Laser-induced transient conversion of rhodochrosite/polyimide into multifunctional MnO₂/graphene electrodes for energy storage applications, *J. Colloid Interf. Sci.* 653 (2024) 606–616.
- [39] Q. Li, Q. Li, Z. Wang, X. Zheng, S. Cai, J. Wu, Recent Advances in Hierarchical Porous Engineering of MOFs and Their Derived Materials for Catalytic and Battery: Methods and Application, *Small* 20 (8) (2024) 2303473.
- [40] W. Chen, C. Ge, J.T. Li, J.L. Beckham, Z. Yuan, K.M. Wyss, P.A. Advincula, L. Eddy, C. Kittrell, J. Chen, Heteroatom-doped flash graphene, *ACS Nano* 16 (4) (2022) 6646–6656.
- [41] H. Liu, W. Shi, Y. Guo, Y. Mei, Y. Rao, J. Chen, S. Liu, C. Lin, A. Nie, Q. Wang, Supersaturated Doping-Induced Maximized Metal-Support Interaction for Highly Active and Durable Oxygen Evolution, *ACS nano* (2024).
- [42] Q. Han, W. Zhang, Z. Han, F. Wang, D. Geng, X. Li, Y. Li, X. Zhang, Preparation of PAN-based carbon fiber@MnO₂ composite as an anode material for structural lithium-ion batteries, *J. Mater. Sci.* 54 (18) (2019) 11972–11982.
- [43] L. She, B. Zhao, M. Yuan, J. Chen, B. Fan, H. Pan, R. Che, Joule-heated flexible carbon composite towards the boosted electromagnetic wave shielding properties, *Adv. Compos. Hybrid Mater.* 5 (4) (2022) 3012–3022.
- [44] H. Zhang, L. Lin, B. Wu, N. Hu, Vertical carbon skeleton introduced three-dimensional MnO₂ nanostructured composite electrodes for high-performance asymmetric supercapacitors, *J. Power Sources* 476 (2020) 228527.
- [45] J. Wang, J.-G. Wang, H. Liu, C. Wei, F. Kang, Zinc ion stabilized MnO₂ nanospheres for high capacity and long lifespan aqueous zinc-ion batteries, *J. Mater. Chem. A* 7 (22) (2019) 13727–13735.
- [46] S. Parveen, S. Pandey, Electrochemical study of 3D hierarchical dandelion-fiber flake-like structure of Al(OH)₃/MnO₂ nanocomposite thin film for future supercapacitor applications, *Electrochim. Acta* 319 (2019) 832–842.
- [47] H. Liu, H. Shi, L. Guo, Z. Fang, D. Chen, W. Li, B. Deng, W. Li, K. Du, H. Yin, Enhanced Graphitization of CO₂-Derived Carbon Anodes via Joule Heating Reformation for High-Performance Lithium-Ion Batteries, *Carbon* 119781 (2024).
- [48] G. Wang, Y. Sun, D. Li, W. Wei, X. Feng, K. Müllen, Constructing Hierarchically Hollow Core-Shell MnO₂/C Hybrid Spheres for High-Performance Lithium Storage, *Small* 12 (29) (2016) 3914–3919.
- [49] Y. Xu, X. Ye, Y. Qiu, C. Gan, L. Huang, X. Tang, X. Luo, A Novel Co₃O₄/MnO₂/C Electrode with Hierarchical Heterostructure for High-performance Lithium-Ion Batteries, *ChemistrySelect* 5 (44) (2020) 13831–13836.
- [50] H. Liang, Y. Liu, J. Hong, X. Huang, In-Situ Growth of Sandwich-Like Ultrathin MnO₂/Carbon/MnO₂ Composite for Fast and Stable Kinetic Process of Lithium Storage, *ACS Appl. Energy Mater.* 7 (4) (2024) 1573–1582.
- [51] M. Song, Y. Liu, J. Hong, X. Wang, X. Huang, Boosting bidirectional conversion of polysulfide driven by the built-in electric field of MoS₂/MoP Mott-Schottky heterostructures in lithium-sulfur batteries, *J. Adv. Ceram* 12 (2023) 1872–1888.
- [52] H. Liang, Y. Liu, M. Song, X. Wang, Y. Song, X. Huang, A two-step strategy for the preparation of ultra-small Mn₃O₄@C anode for lithium-ion batteries, *J. Alloys Compd.* 976 (2024) 173037.
- [53] M. Song, Y. Liu, X. Wang, H. Liang, J. Hong, B. Zhu, D. Jia, X. Huang, Y. Zhou, Atomic substitution engineering-induced domino synergistic catalysis in Li-S batteries, *Chem. Eng. J.* 502 (2024) 157926.
- [54] W. Xi, J. Zhang, Y. Zhang, R. Wang, Y. Gong, B. He, H. Wang, J. Jin, A 3D-printed Al metal-organic framework/S cathode with efficient adsorption and redox conversion of polysulfides in lithium-sulfur batteries, *J. Mater. Chem. A* 11 (14) (2023) 7679–7689.
- [55] X. Zheng, Y. Qiu, J. Luo, S. Yang, Y. Yu, Z. Liu, R. Zhang, C. Yang, Perfluorinated Amines: Accelerating Lithium Electrodeposition by Tailoring Interfacial Structure and Modulated Solvation for High-Performance Batteries, *Small* 20 (44) (2024) 2404614.
- [56] B. Li, W. Zhang, K. Yang, L. Li, J. Luo, Q. Lin, Y. Li, Z. Liu, L. Li, Y. Yu, Bridging Atomic and Macroscopic Perspectives on Heteroepitaxial Growth in Lithium Metal Anodes, *ACS Energy Lett.* 9 (10) (2024) 5215–5224.
- [57] J. Luo, Q. Huang, D. Shi, Y. Qiu, X. Zheng, S. Yang, B. Li, J. Weng, M. Wu, Z. Liu, Dynamic Interfacial Protection via Molecularly Tailored Copolymer for Durable Artificial Solid Electrolyte Interphase in Lithium Metal Batteries, *Adv. Funct. Mater.* 2403021 (2024).